



# Facile scalable synthesis of ordered macroporous few-layer MoS<sub>2</sub> and carbon hybrid nanoarchitectures with sodium-ion batteries

Xiaoxuan Ma<sup>1</sup> · Shikun Liu<sup>1</sup> · Kun Zhang<sup>1</sup> · Xusong Liu<sup>1</sup> · Jian Hao<sup>1</sup> · Caixia Chi<sup>1</sup> · Jiupeng Zhao<sup>1</sup> · Xiaoxu Liu<sup>1,2</sup> · Yao Li<sup>3</sup>

Received: 24 October 2017 / Accepted: 15 November 2017 / Published online: 7 December 2017  
© Springer Science+Business Media, LLC, part of Springer Nature 2017

## Abstract

Heterogeneous interfaces interaction and multiscale nanostructures in two-dimensional (2D) materials hybrids are critically significant for realizing rate capability and long-life cycling performance. However, to strike a balance between minimizing the carbon content and maximizing the heterogeneous interfaces remains a critical challenge in nanoarchitectures for hybrid few-layers MoS<sub>2</sub> with various carbonaceous materials. Here we present the ordered macroporous few-layered MoS<sub>2</sub>/C hybrid nanoarchitectures via a facile scalable in situ hybridization and spatial confinement strategies. Such hybrid strategies can maximize the MoS<sub>2</sub> loading and restriction of MoS<sub>2</sub> to a ultras-small reaction. The optimized as-prepared hierarchical MoS<sub>2</sub>/C hybrids exhibit an initial capacity up to 631.2 mAh g<sup>-1</sup> with a high first columbic efficiency of 81.16% for sodium-ion batteries (SIBs) at 200 mA g<sup>-1</sup>. And, the electrodes display a high reversible capacity of 330.4 mAh g<sup>-1</sup> with a long cycle life, superior cycling stability and excellent high-rate performance demonstrated rational designed hybrid architecture using as the electrodes in SIBs. This strategy could be proven to be an effective method for stabilizing the cyclability and improving in rechargeable rate performance for SIBs.

## 1 Introduction

In the past several years, rechargeable SIBs have attracted worldwide focus and exploration owing to their earth-abundant natural resources, low cost and enhanced safety characteristics [1–10]. Compared to lithium-ion batteries

(LIBs), intrinsic limitations of SIBs are that Na<sup>+</sup> own a much larger ionic radius (Na 1.02 vs. Li 0.76 Å) and more significant ionization [11–18]. Suffering from these negative factors, SIBs present dramatic impact on the electrode crystal structure, the low voltage, fast capacity fading and poorly reversible capacities. To overcome these drawbacks, the ideal electrodes need to possess characteristics of both rapid ion diffusion and higher capacities [19].

The molybdenum disulfides (MoS<sub>2</sub>) becomes a “shining star” as anode electrode candidates for SIBs, because of the unique layered structure with large interlayer spacing (0.62 nm) [20–23]. This structure character can benefit the Na<sup>+</sup> diffusion kinetics and the conversion reaction (MoS<sub>2</sub> to metal Mo and Na<sub>2</sub>S) could enable high theoretical capacity [24, 25]. However, the low utilization of MoS<sub>2</sub> caused by low electronic conductivity limits its further application [26]. The nano-sized MoS<sub>2</sub> tend to restack and pulverization in cycling, decreasing the reversible capacity. Furthermore, the dissolved loss of active sulfur is not an ignored negative factor for the capacity retention [27]. To solve these problems, the previous explorations mostly focus on coated MoS<sub>2</sub> onto various carbon materials such as graphene [28], carbon nanotube [29], carbon sphere [30] and carbon fiber cloth [31]. These nanocomposites have already been

**Electronic supplementary material** The online version of this article (<https://doi.org/10.1007/s10854-017-8283-6>) contains supplementary material, which is available to authorized users.

✉ Jiupeng Zhao  
jiupengzhao@126.com

✉ Xiaoxu Liu  
liu88062321@163.com

✉ Yao Li  
yaoli@hit.edu.cn

<sup>1</sup> School of Chemistry and Chemical Engineering, Harbin Institute of Technology, Harbin 150001, People's Republic of China

<sup>2</sup> Heilongjiang University of Science and Technology, Harbin 150022, People's Republic of China

<sup>3</sup> Center for Composite Materials and Structure, Harbin Institute of Technology, Harbin 150001, People's Republic of China

demonstrated that a synergistic effect on relatively enhanced rate performance and increased cycling stability. In spite, that the obviously tremendous progress of some excellent reported MoS<sub>2</sub>-carbon nanocomposites has been achieved on this front, cycling performance and sodium storage capacity are far from satisfactory. How to make full utilization of MoS<sub>2</sub>-carbon heterogeneous interfaces, offer adequate electric and chemical coupling bridging MoS<sub>2</sub> and carbon are still facing a significant challenge [32]. An effective strategy to address these issues is to embed few-layers or single-layer MoS<sub>2</sub> in conductive carbon materials through the construction of hierarchical hybrid architectures. For example, Yu and co-workers found that the hybrid fiber with single-layered MoS<sub>2</sub> encapsulated in carbon matrix demonstrated outstanding sodium storage and remarkable cycling stability, which achieved the capacity of 484.0 at 1.0 A g<sup>-1</sup> for BILs after 100 cycles [33]. The restriction of MoS<sub>2</sub> to ultrathin reaction results in a remarkable cycling performance. Chen's group synthesized few-layers MoS<sub>2</sub> nanosheets hybrid with carbon embedded in the microspheres full with mesoporous by spraying pyrolysis method. After 2500 cycles, the as-synthesized hybrids demonstrated a capacity of 390 mAh g<sup>-1</sup> at 1.0 A g<sup>-1</sup> and superior high rate ability. The excellent electrochemical performance can due to the rational design of the few-layers MoS<sub>2</sub> nanosheets reaction confined by carbon in microspheres [34]. Zhu et al. reported few-layered MoS<sub>2</sub> and carbon composite nanotube by a facile hydrothermal method. This composite displayed a capacity retention of 90% after 300 cycles at 0.5 A g<sup>-1</sup>. The improved cycling stability could be attribute to the restriction of few-layers MoS<sub>2</sub> dissolved in electrolyte and stable hollow composite structure [35]. In such MoS<sub>2</sub>/C hybrids, rationally designed hybrids architectures with minimized phase separation and maximized heterogeneous interfaces have been recognized as the key to solving the problems [29]. Precise scalable control in few-layers or single-layer MoS<sub>2</sub> hybrids synthesis and spontaneous construction of hierarchically nano-architectures are challenging but significant in the practical implementation.

Herein, we developed a facile scalable synthesis approach to fabricate ordered macroporous few-layered MoS<sub>2</sub>/C hybrid nanoarchitectures (OM-FM/C-HN) by in situ hybridization and spatial confinement strategies. The as-synthesized architecture possesses a three-dimensional ordered macroporous structure with thin hybrid nanowalls full of mesoporous pores, which endows the effective electrolyte infiltration and maintains high diffusion mobility of Na<sup>+</sup>. The electrochemistry can be stabilized by few-layers MoS<sub>2</sub> homogeneously distribute and confinement in amorphous carbon walls, greatly increasing heterogeneous interfaces areas and effective isolating MoS<sub>2</sub> phase. The products have manifested the merits of an outstanding anode for SIBs: The optimized as-prepared hierarchical MoS<sub>2</sub>/C hybrids exhibit an initial

capacity of 631.2 mAh g<sup>-1</sup> with a high first columbic efficiency of 81.16% for BILs at 200 mA g<sup>-1</sup>. For the electrode, high reversible capacity of 330.4 mAh g<sup>-1</sup> can be achieved with the capacity retention of 55.46% after 1000 cycles. This electrode in SIBs with superior cycling stability and excellent high-rate performance demonstrates the rational designed hybrid architecture.

## 2 Experimental section

### 2.1 Preparation of ordered macroporous MoS<sub>2</sub> (OM MoS<sub>2</sub>)

SiO<sub>2</sub> colloidal microspheres were prepared via the Stöber method with a diameter of 420 nm [36]. The SiO<sub>2</sub> microspheres were dispersed in ethanol and close-packed into colloidal crystals by centrifugation (3000 rpm, 10 min). After the SiO<sub>2</sub> template sintered at 850 °C for 20 min in air to improve the mechanical strength, the interstitial spaces between the SiO<sub>2</sub> microspheres were filled by 0.2 g (NH<sub>4</sub>)<sub>6</sub>Mo<sub>7</sub>O<sub>24</sub>·4H<sub>2</sub>O and 0.21 g CH<sub>4</sub>N<sub>2</sub>S solution in 20 ml ethanol, followed by vacuum drying at 78 °C for 24 h. The composite was placed in the middle of the furnace tube and heated at 750 °C for 2 h under Ar. After natural cooling, the composite was immersed in 5% HF solution for 2 h to remove the SiO<sub>2</sub> template. OM MoS<sub>2</sub> was then obtained by centrifugation and washed with deionized water.

### 2.2 Preparation of OM-FM/C-HN

The interstitial spaces between the sintered SiO<sub>2</sub> microspheres were filled by 0.2 g (NH<sub>4</sub>)<sub>6</sub>Mo<sub>7</sub>O<sub>24</sub>·4H<sub>2</sub>O, 0.21 g CH<sub>4</sub>N<sub>2</sub>S and varying weight citric acid solution in 20 ml ethanol, followed in vacuum at 80 °C for 24 h. For comparison, different masses citric acid of 0.2, 0.6 and 1.2 g were used to prepare OM-FM/C-HN. The samples were denoted as OM-FM/C-HN1, OM-FM/C-HN2 and OM-FM/C-HN3 respectively. The synthesis procedure of ordered macroporous carbon (OMC) as reference sample was similar with that of OM-FM/C-HN but the interstitial spaces between the SiO<sub>2</sub> microspheres were filled by 1.6 g citric acid and 0.35 g concentrated sulfuric acid solution in 20 ml water, followed in vacuum at 80 °C for 24 h.

### 2.3 Materials characterizations

The morphology of the hybrids was collected on Hitachi S-4800 with an acceleration voltage of 20 kV, Transmission electron microscopy (TEM), High-resolution transmission electron microscopy (HRTEM) images and selected-area electron diffraction (SAED) patterns were characterized by a JEOL JEM-2010. The crystal phase of the hybrids was

recorded by Max-2500 X-ray diffraction on Cu K $\alpha$  X-ray source. Raman spectra were collected on a WITec Raman microscopy system (CRM 200 confocal). The surface composition and chemical environment of the hybrids were analyzed via PHI-5000 VersaProbe (Kratos Axis Ultra Al on 14 kV). Brunauer–Emmet–Teller (BET) surface areas were measured using NOVA 2000 (Quantachrome, USA) instrument to measure the adsorption of nitrogen. The pore size distribution curves were calculated from the isotherm using the Barrett–Joyner–Halenda (BJH) algorithm. The MoS<sub>2</sub> loading mass was carried out on Thermo-Gravimetric Analyzer with a PerkinElmer Pyris 6 at a heating rate of 15 °C/min in air.

## 2.4 Electrochemical measurements

Coin cells were fabricated by assembly of 2016 coin-type cells in a pure argon gas filled glove box. The hybrids electrode was made by homogeneously slurring the mixture of active material (70 wt%), carbon blacks (20 wt%), and PVDF (10 wt%) with *N*-methyl-2-pyrrolidone on Cu foil. For SIBs fabrication, the metallic Na foil was carried out as the counter-electrode, 1.0 mol L<sup>-1</sup> NaPF<sub>6</sub> in ethylene carbonate (EC)/diethyl carbonate (DEC)/fluoroethylene carbonate (FEC) (1:1:0.05 v v<sup>-1</sup>) was used as the electrolyte, and microporous glass fiber as the separator. Galvanostatic charge/discharge measurement was tested on a NEWARE BTS-610 (Newware Technology Co., Ltd., China) at room temperature. Electrochemical workstation (CHI660E, Shanghai Chenhua Co., Ltd., China) was used to test cyclic voltammetry (CV) and electrochemical impedance spectroscopy (EIS).

## 3 Results and discussion

The general electrode fabrication protocol is illustrated in Fig. 1. First, the SiO<sub>2</sub> colloidal crystal template was obtained after centrifuged at 3000 rpm and sintered at 800 °C in air (Fig. 1a, b). Then the precursor was impregnated into the channels of SiO<sub>2</sub> colloidal crystal template. Finally, MoS<sub>2</sub> and carbon hybrids were in situ produced in the gaps of the template after calcination. After selective removal of the SiO<sub>2</sub> colloidal template, the ordered macroporous structure with replicated ordered structure of the colloidal crystal template was produced (Fig. 1d).

As shown in Fig. 2a, the SEM exhibits morphology of the SiO<sub>2</sub> colloidal crystal template, which presents well-ordered close packed array with an average center-to-center distance about 420 nm. As the ordered macroporous structure is replicated from colloidal crystal, the as-prepared carbon and MoS<sub>2</sub> composites exhibit honeycomb-like structure (Fig. 2b–f). Interestingly, this structure indicates that two nanoscale pores: macropores with the sizes similar to the

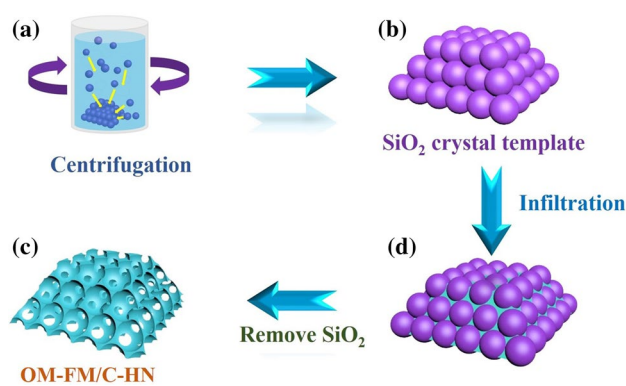


**Fig. 1** Schematic illustration for the fabrication of the OM-FM/C-HN electrodes

morphology of SiO<sub>2</sub> spheres and mesopores with tens of nanometers formed by the contact spheres points. The SEM image of OM MoS<sub>2</sub>, OM-FM/C-HN1, OM-FM/C-HN2, OM-FM/C-HN3 and OMC demonstrate the well-ordered nanostructure progressively deforms with increasing carbon contents (Fig. 2b–f). This degradation of the ordered structure could be due to the volumetric shrinkage of citric acid at high temperature carbonization.

Figures 3a, S1 and S2 show TEM images of the macroporous and mesoporous structure of OM MoS<sub>2</sub>, OM-FM/C-HN1, OM-FM/C-HN2, OM-FM/C-HN3 and OMC. The pore sizes of these materials well conform to the SEM images. EDX line-scan profiles of Mo (red), S (green), C (yellow) were taken across the nanoarchitecture of OM-FM/C-HN1, which unambiguously confirms the existence and homogeneous distribution of Mo, S, and C within the ordered macroporous nanoarchitecture (Fig. 3b). The EDX mapping result also gives a strong evidence of uniform distribution of Mo, S, and C elements on the nanoarchitecture in Fig. S3. Figure 3c, d reveal amorphous carbon and few-layers MoS<sub>2</sub> layers distribute on the walls full with mesoporous in OM-FM/C-HN1. The interlayer spacing of the MoS<sub>2</sub> (002) layers are measured about 0.81–0.99 nm in Fig. 1d, which is much larger than the OM MoS<sub>2</sub> crystal of 0.63 nm. The expansion of interlayer (002) planes distance can be mainly attributed to the involvement of carbon molecules into the MoS<sub>2</sub> interlamination, indicating the relatively strong interfacial interaction between amorphous carbon and MoS<sub>2</sub>. The inset of Fig. 3d is the selected area electron diffraction (SAED) patterns. The ring patterns indicate polycrystalline phase of disorder distributed MoS<sub>2</sub> layers, and the patterns are indexed as a typical MoS<sub>2</sub> hexagonal phase (P63/mmc). Figure 3e, f indicate the polycrystalline nature of OM MoS<sub>2</sub> and obviously lower density of mesopores in the MoS<sub>2</sub> architecture. The interlayer distance of (002) layers is 0.63 nm in OM MoS<sub>2</sub>, which shows more orderly and narrow than that of OM-FM/C-HN1 (Fig. 3f). The inset of Fig. 3f shows the

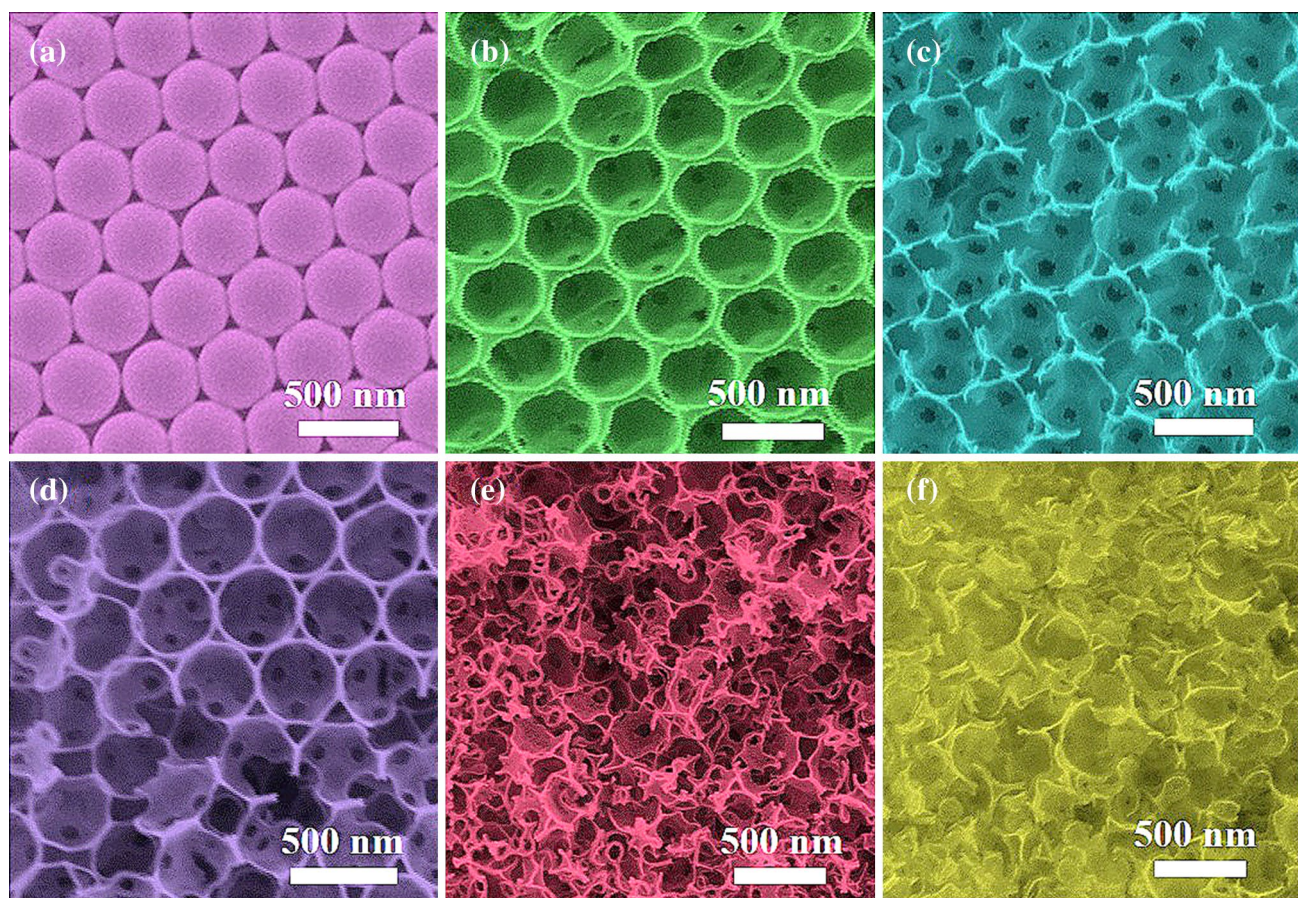


**Fig. 2** SEM images of electrodes: **a** SiO<sub>2</sub> crystal template. **b–f** OM MoS<sub>2</sub>, OM-FM/C-HN1/2/3, OMC electrodes

SAED pattern of OM MoS<sub>2</sub>, the sharper ring patterns further confirm OM MoS<sub>2</sub> with higher crystallinity than OM-FM/C-HN1. Compared with OM-FM/C-HN1, the hybrid architecture of OM-FM/C-HN2 owns more disordered and fewer layers packing MoS<sub>2</sub> layers (Fig. S2b, c). As the increasing contents of carbon, there are just many shorten and single-layer MoS<sub>2</sub> thin layers distributed on the hybrid architecture of OM-FM/C-HN3 (shown in Fig. S2f).

BET and BJH were respectively shown in Fig. S4a, b. The pore size distribution reveals that as-prepared electrodes possess 20–40 nm mesopores shown in TEM and 2–5 nm mesopores observed in HRTEM. The specific surface area and total pore volume of the electrodes gradually increase with the increasing of carbon content (Fig. S4c). This phenomenon may be ascribed to the volume shrinkage by pyrolysis of citric acid, the higher weight rate of citric acid, the greater volume shrinkage of the composite. And, this effect not only leads to the well-ordered nanostructure deformation but mesopores generation. The volumetric shrinkage phenomenon leaves lots of mesopores among the walls [37].

The crystallinity and crystal phases of the hybrids have been investigated by X-ray diffraction analysis. As the

XRD patterns shown in Fig. 4a, four characteristic diffraction peaks (002), (100), (103) and (110) from 2H-MoS<sub>2</sub> (JCPDS # 37-1492) and two diffraction peaks (002) and (100) from carbon could be observed dominantly. Notably, the OM MoS<sub>2</sub> exhibits a strong and sharp (002) diffraction at 14.45° with a *d*-spacing of 0.63 nm, while the OM-FM/C-HN1 shows a weak and broad (002) diffraction centered at 9.47° with a *d*-spacing of 0.96 nm. The results suggest the arrangement of S–Mo–S layers become disordered, and the interlayer spacing of adjacent MoS<sub>2</sub> layers be enlarged. From OM MoS<sub>2</sub> to OM-FM/C-HN3, the crystalline peaks (100), (103) and (110) corresponding to 2H–MoS<sub>2</sub> diffraction peaks become broaden and its (002) diffraction peaks disappears. The increasing amorphous carbon percentage can lead to the decrease crystallinity of 2H–MoS<sub>2</sub> [38]. Compared with OM-FM/C-HN1, the decreased crystallinity can be interpreted by more single-layer MoS<sub>2</sub> with larger interlayer spacing more disorderly disperse in the carbon matrix in OM-FM/C-HN2. The peak intensity of carbon is far stronger than that of MoS<sub>2</sub> for OM-FM/C-HN3, which indicates the single layer of ultra-small MoS<sub>2</sub> distributed in the architecture. The characteristics obtained by XRD

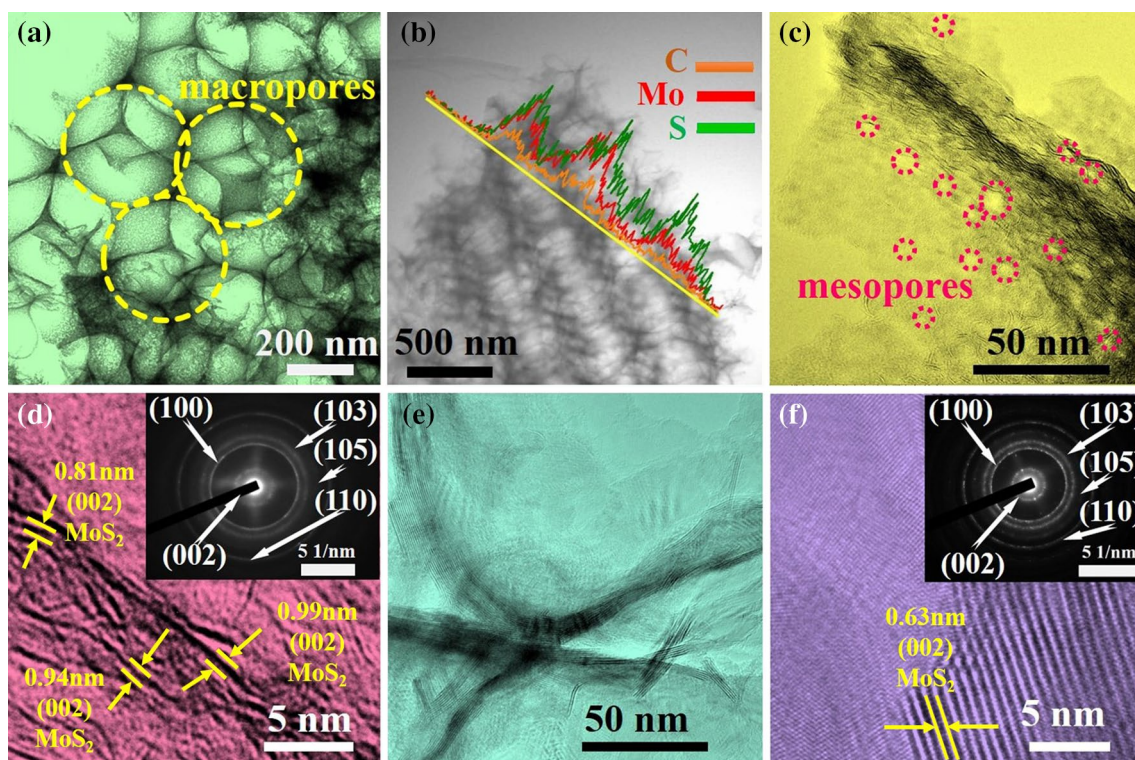


**Fig. 3** **a** Low-resolution TEM image of OM-FM/C-HN1. **b** TEM image of OM-FM/C-HN1 and EDX line-scan profile of Mo (red), S (green), C (yellow). **c** high-resolution TEM image of OM-FM/C-

HN1. **d** HRTEM image of OM-FM/C-HN1, inset depicts SAED pattern of OM-FM/C-HN1. **e** TEM image of OM MoS<sub>2</sub>. **f** HRTEM image of OM MoS<sub>2</sub>, inset depicts SAED pattern of OM MoS<sub>2</sub>

is in good agreement with the HRTEM observation. The hybrid samples in Fig. 3b exhibit four characteristic peaks of amorphous carbon at 1380 (D band), 1590 (G band), 2685 (2D band) and 2870 cm<sup>-1</sup> (2G band). The intensity of carbon peaks become higher with the increasing of carbon content [39]. Meanwhile, two prominent peaks of MoS<sub>2</sub> at ≈ 383 (E<sub>12g</sub> mode) and ≈ 403 (A<sub>1g</sub> mode), are observed. Furthermore, the Raman spectroscopy of MoS<sub>2</sub>-related part is shown in Fig. 3c. In comparison with OM MoS<sub>2</sub>, A<sub>1g</sub> modes of the MoS<sub>2</sub>/C hybrids show blue-shifts and the E<sub>12g</sub> modes suggest red-shifts. As the E<sub>12g</sub> and A<sub>1g</sub> modes of MoS<sub>2</sub> are highly sensitive to molecule interaction and intra-layer bonding, the frequencies ( $\Delta$ ) difference between the E<sub>12g</sub> and A<sub>1g</sub> modes is one of the significant indicators for the number of MoS<sub>2</sub> layers [40]. These values are calculated to be about 24.9 cm<sup>-1</sup> for OM MoS<sub>2</sub>, 22.0 cm<sup>-1</sup> for OM-FM/C-HN1, 21.4 cm<sup>-1</sup> for OM-FM/C-HN2 and 20.3 cm<sup>-1</sup> for OM-FM/C-HN3 by measuring the Raman spectra. The  $\Delta k$  values of the two peaks for the hybrids are between 22.0 and 20.3 cm<sup>-1</sup> (close to 20.2–21.2 cm<sup>-1</sup> of MoS<sub>2</sub> single layer), supporting the presence of single-layer MoS<sub>2</sub> and few-layers MoS<sub>2</sub> (less than 4 layers) [41].

The XPS was also applied to analyze the atomic valence states and the composition for the five samples in Figs. 4d, e and S5. The XPS spectra of OM-FM/C-HN1 demonstrate

that the peaks of C, O, Mo, and S can be clearly found in Fig. S5a. Observation of Mo<sup>4+</sup> 3d<sub>5/2</sub> and Mo<sup>4+</sup> 3d<sub>3/2</sub> peaks at binding energies of 229.2 and 232.6 eV in Fig. 4d, which are indicated the presence of Mo<sup>4+</sup> state of Mo in MoS<sub>2</sub>, while the binding energies at 162.1 eV (S 2p<sub>3/2</sub> state) and 163.7 eV (S 2p<sub>1/2</sub> state) in S 2p spectrum are correspond well to S<sup>2-</sup> in MoS<sub>2</sub> (Fig. 3d) [42]. From OMC to OM MoS<sub>2</sub> (Fig. S5a), the intensity of the carbon peaks is weaker in the spectrum with decreasing carbon contents in the electrodes (Fig. S5a, b) [43, 44]. Curves of TG determine the mass percentage of MoS<sub>2</sub> in the samples. The weight loss of the samples exhibits from 250 to 750 °C relative to the oxidation of MoS<sub>2</sub> and the combustion of carbon (Fig. 4f). The retained weight percentages of OM MoS<sub>2</sub>, OM-FM/C-HN1, OM-FM/C-HN2, OM-FM/C-HN3 and OMC maintain at 84.10, 68.1, 41.3, 21.0 and 0.1% among 700–750 °C. The MoS<sub>2</sub> contents are calculated to be 99.98, 71, 42, 19 and 0% in electrodes.

The sodium storage properties of OM MoS<sub>2</sub>, OM-FM/C-HN1, OM-FM/C-HN2, OM-FM/C-HN3 and OMC as anode materials were investigated in Fig. 5. Figure 5a is the initial three CV curves of the anode assembled by OM-FM/C-HN1 at a scan rate of 0.2 mV s<sup>-1</sup> between 0.01 and 3.0 V. In the first cathodic process, the curve exhibits three reductive peaks, including abroad bands at 1.03, 0.48V and a sharp peak at 0.11V. The reduction peak around 1.03 V could be

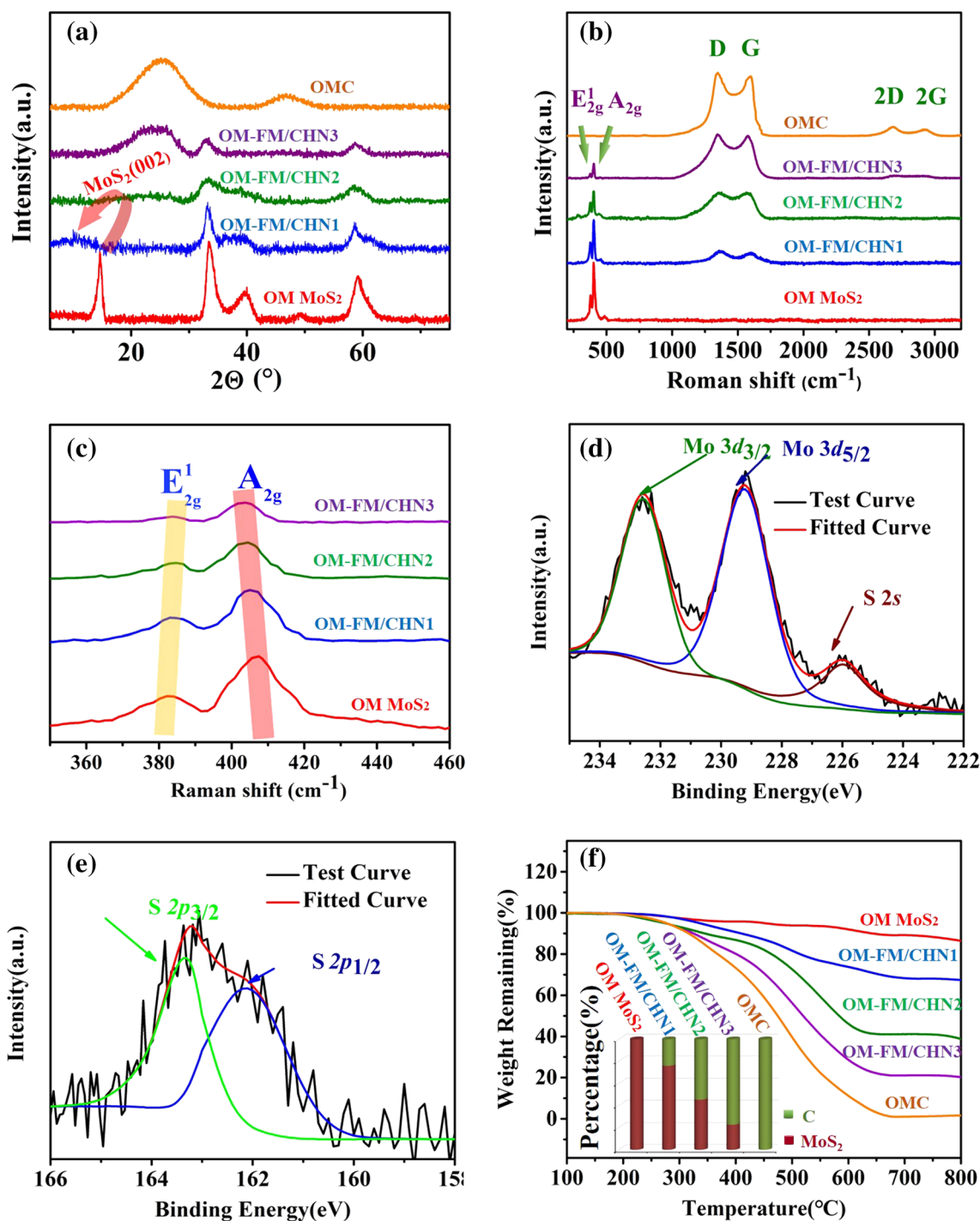


**Fig. 4** a XRD patterns of OM MoS<sub>2</sub>, OM-FM/C-HN1/2/3 and OMC. b Raman spectra of OM MoS<sub>2</sub>, OM-FM/C-HN1/2/3 and OMC. c The magnified Raman spectrum of the composites, showing the peaks of OM MoS<sub>2</sub>, OM-FM/C-HN1/2/3 and OMC. d XPS S1s and Mo 3d

spectrum of OM-FM/C-HN1 e XPS S 2p spectrum of OM-FM/C-HN1. f The TGA curves of OM MoS<sub>2</sub>, OM-FM/C-HN1/2/3 and OMC under air atmosphere, the inset shows the weight contents of MoS<sub>2</sub> and carbon for each electrode

assigned to the insertion of Na<sup>+</sup> ions in 2H–MoS<sub>2</sub> interlayers to form 2H–Na<sub>x</sub>MoS<sub>2</sub> and the continuous Na<sup>+</sup> insertion induced phase transition from 2H-to1T-Na<sub>x</sub>MoS<sub>2</sub> [45]. The reduction peak at 0.48V disappears in subsequent sodiation

progress, indicating this peak is associated with formation of the solid electrolyte interface (SEI) layer on MoS<sub>2</sub>, which leads to an irreversible capacity loss in the first cycle. The peak below 0.30 V corresponds to the following conversion

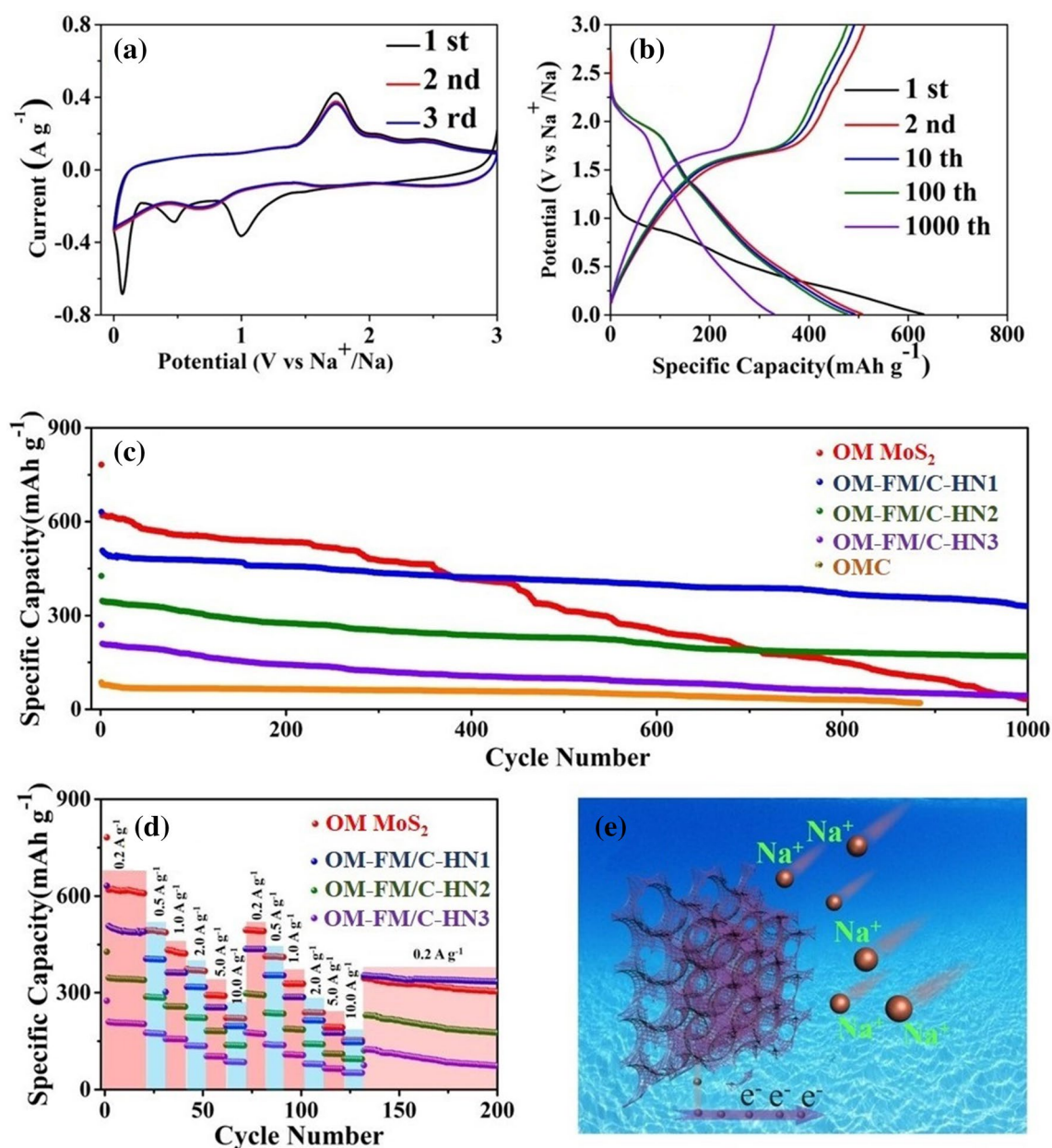


**Fig. 5** **a** CV curves of the first three cycles of the OM-FM/C-HN1 electrode at a current density of  $0.2 \text{ A g}^{-1}$  as anode material for sodium ion battery. **b** The first three galvanostatic charge–discharge profiles of the OM-FM/C-HN1 electrode at a current density of  $0.2 \text{ A g}^{-1}$  in the voltage range of 0.01–3.0 V vs.  $\text{Na}^+/\text{Na}$ . **c** Cycling performance of OM  $\text{MoS}_2$ , OM-FM/C-HN1/2/3 and OMC electrodes

reaction from  $\text{Na}_x\text{MoS}_2$  to Mo and  $\text{Na}_2\text{S}$  [46]. A strong oxidation peak at 1.75 V indicates the  $\text{Na}_2\text{S}$  into S and  $\text{Na}^+$ , revealing the conversion reaction of oxidation of the Mo nanograins to  $\text{MoS}_2$  [47]. From the 2nd discharge cycle, there are three broad peaks for 1.55–2.21, 0.48–1.18, and 0–0.30 V, respectively. In the following oxidation curves, the peaks near 1.75 V correspond to the desodiation of  $\text{Na}_2\text{S}$  [48]. The CV curves of the 2nd and 3rd cycle are nearly

at a current density of  $0.2 \text{ A g}^{-1}$ . **d** Multi-rate testing of OM  $\text{MoS}_2$  and OM-FM/C-HN1/2/3 at discharge current densities of 0.2, 0.5, 1.0, 2.0, 5.0, 10.0, 0.2, 0.5, 1.0, 2.0, 5.0, 10.0 and  $0.2 \text{ A g}^{-1}$ . **e** Schematic of the electrolyte ion diffusion and fast electron transport in M-FM/C-HN1

overlapped, demonstrating its high reversibility and cycling stability.

Charge/discharge curves of the hybrid electrodes at 1st, 2nd, 10th, 100th and 1000th cycles in the voltage range of 0.01–3.0 V at a constant current density of  $0.2 \text{ A g}^{-1}$  are displayed in Figs. 5b and S6. The initial discharge and charge capacities are 631.2 and 512.3  $\text{mAh g}^{-1}$ , respectively, and corresponding initial coulombic efficiency is 81.16%.

The relatively higher initial coulombic efficiency can be ascribed to decreased dissolution of soluble polysulfides. The reversible discharge capacity of the OM-FM/C-HN1 is  $350.1 \text{ mAh g}^{-1}$ , and the coulombic efficiency remains above 99% in the 1000th cycles. (Figs. 5b and S6). The superior long-term cyclability is a significant and crucial factor for promising anode electrodes for rechargeable SIBs. The challenges lie in the insertion/extraction of the large  $\text{Na}^+$  radius within the active materials and side reactions on the interface of electrode and the electrolyte. The cycling stability of the electrodes is presented in Figs. 5c and S7 for comparison. The OM-FM/C-HN1 electrode exhibits an initial capacity of  $631.2 \text{ mAh g}^{-1}$  with an initial coulombic efficiency of 81.16%, whereas the initial capacity of OM  $\text{MoS}_2$  is about  $782.4 \text{ mAh g}^{-1}$  with an initial coulombic efficiency of 79.87% (Figs. 5c and S7). The OM-FM/C-HN1 electrode could still reach  $330.4 \text{ mAh g}^{-1}$  in reversible specific capacity with slow capacity fading after 1000 cycles, prominently higher than those for OM  $\text{MoS}_2$ , OM-FM/C-HN2 and OM-FM/C-HN3, respectively (Fig. S7b). In sharp contrast with OM-FM/C-HN1 displaying excellent long-term cyclability, OM  $\text{MoS}_2$  delivers a reversible capacity fades rapidly to merely  $33.2 \text{ mAh g}^{-1}$  after 1000 cycles (Figs. 5c and S7a). Such findings imply that the amorphous carbon well confine few-layers  $\text{MoS}_2$  play a significant role in maintaining long-term cyclability of  $\text{MoS}_2$ . As shown in Figs. 5c and S7b, the reversible capacity retention of the OM-FM/C-HN2 could be maintained at  $170.6 \text{ mAh g}^{-1}$  after 1000 cycles. However, the OM-FM/C-HN3 drops to only  $44.2 \text{ mAh g}^{-1}$  after 1000 cycles caused by the lowest percentage of  $\text{MoS}_2$  among the architecture (Figs. 5c, S7c, d). Compared with OM-FM/C-HN2, OM-FM/C-HN3 and OMC, OM-FM/C-HN1 owns the highest reversible capacity due to the highest percentage of  $\text{MoS}_2$  in the electrodes. Figure 5d compares the rate performances of the electrodes, where the current density is up to  $10.0 \text{ A g}^{-1}$  from  $200 \text{ mA g}^{-1}$ . As shown in Fig. 5d, the capacities of OM-FM/C-HN1 at current densities of 0.2, 0.5, 1.0, 2.0, 5.0, 10.0, 0.2, 0.5, 1.0, 2.0, 5.0, 10.0 and  $0.2 \text{ A g}^{-1}$  are 489.1, 403.4, 361.7, 317.2, 254.3, 196.4, 435.4, 353.6, 286.3, 213.9, 175.6, 146.7 and  $350.3 \text{ mAh g}^{-1}$ , respectively. It is clear that the OM-FM/C-HN1 anode has better rate capability than OM  $\text{MoS}_2$ , resulting of lower barrier for migration of  $\text{Na}^+$  and electrons, caused by shorten the  $\text{Na}^+$  diffusion distances in nanoscale architecture. It also indicates that the OM-FM/C-HN1 remains very stable during the extended rate cycling process. Comparing the pristine  $\text{MoS}_2$ , OM  $\text{MoS}_2$  shows better cycling stability and rate performance, demonstrated the suitable structural superiority and restriction of  $\text{MoS}_2$  to ultrasmall reaction (in Fig. S8). The high reversible capacities, outstanding first coulombic efficiency, enhanced rate capability, and excellent cycling stability of the OM-FM/C-HN1 electrode are impressive when compared to many previously reported

$\text{MoS}_2$ -based electrodes, as shown in Table S1. As shown in Fig. S9a, the OM-FM/C-HN1 still maintains the morphology of macroporous structure after cycled. This indicates the excellent stability of macroporous structure. And, the  $\text{MoS}_2$  presents amorphous crystals (Fig. S9b, c).  $\text{MoS}_2$  were uniformly dispersed all over the carbon frameworks without aggregation even after 1000 cycles. The XPS spectrum of OM-FM/C-HN1 and OM  $\text{MoS}_2$  reveal the S/Mo atomic ratio of OM-FM/C-HN1 is measured as 1.8 after cycled in Fig. S9d. However, the S/Mo atomic ratio of OM  $\text{MoS}_2$  is measured as 1.1 by XPS analysis. This proves that the amorphous carbon surrounding the few layer  $\text{MoS}_2$  effectively block the dissolution of sulfur in OM-FM/C-HN1. Impedance measurements of OM-FM/C-HN1 and OM  $\text{MoS}_2$  were carried out before cycling and after 1000 cycles at a constant current density of  $0.2 \text{ A g}^{-1}$ , as shown Fig. S9e, f. The charge transfer resistances ( $R_{ct}$ ) of OM  $\text{MoS}_2$  and OM-FM/C-HN1 were equal to 61, 87 before cycled and 326, 271 after cycled, respectively. This proves that the amorphous carbon effectively improves the conductivity of OM-FM/C-HN1 in the long cycle.

As illustrated in Fig. 5e, the unique structural characteristics of OM-FM/C-HN1 enhanced long-term cycle stability and the superior rate performance and could be summarized as the following distinct factors: (a) the open and hierarchically pores (providing more exposed active sites and a large contact area); the honeycomb-like structure formed by replicating  $\text{SiO}_2$  template (buffering the large mechanical stress stemming from the volume changes due to the conversion reaction) and hybrid nanosized architecture (avoiding electrode aggregation or stacking/restacking of  $\text{MoS}_2$ ); (b) In situ hybridization results in effective isolation of  $\text{MoS}_2$  to the ultrasmall reaction by amorphous carbon and constructing large  $\text{MoS}_2$ /carbon heterogeneous interfaces. There are a large number of defect sites and vacancies exists on the heterogeneous interfaces, which can facilitate the  $\text{Na}^+$  storage and diffusion. (c) The amorphous carbon ensures the high electron conductivity and adsorbs/anchors polysulfides, restraining the reaction of  $\text{Na}_2\text{S}$  with electrolyte and the polysulfides shuttle effects. The combination of the novel structure with the abundant hierarchical pores synergistic improves the electrochemical performance of the OM-FM/C-HN1 anode.

In summary, ordered macroporous few-layer  $\text{MoS}_2$  and amorphous carbon hybrid nanoarchitectures have been successfully designed and prepared through a facile scalable in situ hybridization and spatial confinement strategies. The as-synthesized architecture possesses a three-dimensional ordered macroporous structure with the hybrid nanowalls full of mesoporous pores, and few-layers  $\text{MoS}_2$  homogeneously distribution and confinement in amorphous carbon walls. The optimized as-prepared hierarchical  $\text{MoS}_2$ /C hybrids exhibit an initial capacity up to  $631.2 \text{ mAh g}^{-1}$



with a high first columbic efficiency of 81.16% for BILs at 200 mA g<sup>-1</sup>. And, high reversible capacity of 330.4 mAh g<sup>-1</sup> with a long cycle life is achieved, superior cycling stability and excellent high-rate performance demonstrate rational designed hybrid architecture using as the electrodes in SIBs. Our preparation approach could be also widened to the synthesis of few-layers metal sulfide/amorphous carbon hybrids for a wider range of applications in future, such as in sensors, catalysis, and supercapacitors.

**Acknowledgements** The authors would like to acknowledge support from the National Natural Science Foundation of China (Nos. 51502057, 51572058, 51307046, 91216123, 51174063), the Natural Science Foundation of Heilongjiang Province (E201436), the International Science & Technology Cooperation Program of China (2013DFR10630, 2015DFE52770) and Specialized Research Fund for the Doctoral Program of Higher Education (SRFDP 20132302110031), Natural Science Foundation of Heilongjiang Province of China (Grant No. E2016062), the China Postdoctoral Science Foundation (General Financial Grant No. 2014M561345), the Heilongjiang Postdoctoral Science Foundation (LBH-Z14105), the Scientific Research Foundation for the Returned Overseas Chinese Scholars of the State Education Ministry (No. 20151098), the University Nursing Program for Young Scholars with Creative Talents in Heilongjiang province (No. 2015082), and the Open Project Program of the Key Laboratory for Photonic and Electric Band Gap Materials of the Ministry of Education of Harbin Normal University (No. PEBM201405), postdoctoral scientific research developmental fund of Henlongjiang Province (LBH-Q14144), The Research Foundation for the Returned Overseas Chinese excellent Scholars of Heilongjiang Province (No. 2015424), National Key Research & Development Program (2016YFB0303903), and the Foundation of Science and Technology on Advanced Composites in Special Environment Laboratory.

## References

1. A. Liu, H. Lv, H. Liu, Q. Li, H. Zhao, Two dimensional MoS<sub>2</sub>/CNT hybrid ink for paper-based capacitive energy storage. *J. Mater. Sci.-Mater. Electron* **28**(12), 1–8 (2017)
2. X. Ma, X.J. Zhao, J. Hao, C. Chi, X. Liu, Y. Li, S. Liu, K. Zhang, Improved cycling stability of MoS<sub>2</sub>-coated carbon nanotubes on graphene foam as a flexible anode for lithium-ion batteries. *New J. Chem.* **41**(2), 588–593 (2016)
3. Y. Li, X. Wu, J. Song, J. Li, Q. Shao, N. Cao, N. Lu, Z. Guo, Reparation of recycled acrylonitrile-butadiene-styrene by pyromellitic dianhydride: reparation performance evaluation and property analysis. *Polymer* **124**, 41–47 (2017)
4. K. Sun, P. Xie, Z. Wang, T. Su, Q. Shao, J. Ryu, X. Zhang, J. Guo, A. Shankar, J. Li, R. Fan, D. Cao, Z. Guo, Flexible polydimethylsiloxane/multi-walled carbon nanotubes membranous metacomposites with negative permittivity. *Polymer* **125**, 50–57 (2017)
5. X. Zhang, H. Gao, M. Guo, G. Li, Y. Liu, D. Li, A study on key technologies of unmanned driving. *Caai Trans. Intell. Technol.* **1**(1), 4–13 (2016)
6. S. Padhy, S. Panda, A hybrid stochastic fractal search and pattern search technique based cascade PI-PD controller for automatic generation control of multi-source power systems in presence of plug in electric vehicles. *Caai Trans. Intell. Technol.* **2**, 12–25 (2017)
7. X. Xiang, F. Pan, Y. Li, A review on adsorption-enhanced photoreduction of carbon dioxide by nanocomposite materials. *Adv. Compos. Hybrid. Mater.* (2017). <https://doi.org/10.1007/s42114-017-0001-6>
8. S. Aqeel, Z. Huang, J. Walton, C. Baker, D. Falkner, Z. Liu, Z. Wang, Polyvinylidene fluoride (PVDF)/polyacrylonitrile (PAN)/carbon nanotube nanocomposites for energy storage and conversion. *Adv. Compos. Hybrid. Mater.* **7**(10), 1–8 (2017)
9. Z. Sun, L. Zhang, F. Dang, Y. Liu, Z. Fei, Q. Shao, H. Lin, J. Guo, L. Xiang, N. Yerra, Z. Guo, Experimental and simulation understanding of morphology controlled barium titanate nanoparticles under co-adsorption of surfactants. *CrystEngComm* **19**(24), 3288 (2017)
10. T. Liu, K. Yu, L. Gao, H. Chen, N. Wang, L. Hao, T. Li, H. He, Z. Guo, Graphene quantum dots decorated SrRuO<sub>3</sub> mesoporous film as an efficient counter electrode for high-performance dye-sensitized solar cells. *J. Mater. Chem. A* **5**(34), 17848–17855 (2017)
11. G. Huang, T. Chen, W. Chen, Z. Wang, K. Chang, L. Ma, F. Huang, D. Chen, J.Y. Lee, Graphene-like MoS<sub>2</sub>/graphene composites: cationic surfactant-assisted hydrothermal synthesis and electrochemical reversible storage of lithium. *Small* **9**(21), 3693–3703 (2013)
12. Y. Xu, M. Zhou, Y. Lei, Nanoarchitected array electrodes for rechargeable lithium- and sodium-ion batteries. *Adv. Energy Mater.* **6**(10), 1502514 (2016)
13. K. Zhang, G. Li, L. Feng, N. Wang, J. Guo, K. Sun, K. Yu, J. Zeng, T. Li, Z. Guo, M. Wang, Ultralow percolation threshold and enhanced electromagnetic interference shielding in poly(L-lactide)/multi-walled carbon nanotube nanocomposites with electrically conductive segregated networks. *J. Mater. Chem. C* **5**(36), 9359–9369 (2017)
14. X. Lou, C. Lin, Q. Luo, J. Zhao, B. Wang, J. Li, Q. Shao, X. Guo, N. Wang, Z. Guo, Crystal-structure modification enhanced FeNb<sub>11</sub>O<sub>29</sub> anodes for lithium-ion batteries. *ChemElectroChem* **4**, 1–11 (2017)
15. Y. Zheng, Y. Zheng, S. Yang, Z. Guo, T. Zhang, H. Song, Q. Shao, Esterification synthesis of ethyl oleate catalyzed by Brønsted acid–surfactant-combined ionic liquid. *Green Chem. Lett. Rev.* **10**(4), 202–209 (2017)
16. L. Zhang, W. Yu, C. Han, J. Guo, Q. Zhang, H. Xie, Q. Shao, Z. Sun, Z. Guo, Large scaled synthesis of heterostructured electrospun TiO<sub>2</sub>/SnO<sub>2</sub> nanofibers with an enhanced photocatalytic activity. *J. Electrochem. Soc.* **164**(9), H651–H656 (2017)
17. C. Wang, Y. Wu, Y. Li, Q. Shao, X. Yan, C. Han, Z. Wang, Z. Liu, Z. Guo, Flame-retardant rigid polyurethane foam with a phosphorus-nitrogen single intumescent flame retardant. *Polym. Adv. Technol.* (2017). <https://doi.org/10.1002/pat.4105>
18. W. Yang, X. Wang, J. Li, X. Yan, S. Ge, S. Tadakamalla, Z. Guo, Polyoxymethylene/ethylene butylacrylate copolymer/ethylene-methyl acrylate-glycidyl methacrylate ternary blends. *Polym. Eng. Sci.* (2017) <https://doi.org/10.1002/pen.24675>
19. T. Wang, S. Chen, H. Pang, H. Xue, Y. Yu, MoS<sub>2</sub>-based nanocomposites for electrochemical energy storage. *Adv. Sci.* **4**(2), 1600289 (2017)
20. B. Jache, J.O. Binder, T. Abe, P. Adelhelm, A comparative study on the impact of different glymes and their derivatives as electrolyte solvents for graphite co-intercalation electrodes in lithium-ion and sodium-ion batteries. *Phys. Chem. Chem. Phys.* **18**(21), 14299–14316 (2016)
21. F. Tu, X. Xu, P. Wang, L. Si, X. Zhou, J. Bao, A few-layer SnS<sub>2</sub>/reduced graphene oxide sandwich hybrid for efficient sodium storage. *J. Phys. Chem. C* **121**(6), 3261–3269 (2017)
22. Y. Du, X. Zhu, X. Zhou, L. Hu, Z. Dai, J. Bao, Co<sub>3</sub>S<sub>4</sub> porous nanosheets embedded in graphene sheets as high-performance anode materials for lithium and sodium storage. *J. Mater. Chem. A* **3**(13), 6787–6791 (2015)

23. X. Zhou, L. Wan, Y. Guo, Synthesis of MoS<sub>2</sub> nanosheet-graphene nanosheet hybrid materials for stable lithium storage. *Chem. Commun.* **49**(18), 1838–1840 (2013)
24. Y. Zhang, S. Zhao, X. Zeng, TiO<sub>2</sub>-MoS<sub>2</sub> hybrid nano composites with 3D network architecture as binder-free flexible electrodes for lithium ion batteries. *J. Mater. Sci.-Mater. Electron* **28**(13), 1–9 (2017)
25. Y. Teng, H. Zhao, Z. Zhang, Z. Li, Q. Xia, Y. Zhang, L. Zhao, X. Du, Z. Du, P. Lv, K. Swierczek, MoS<sub>2</sub> nanosheets vertically grown on graphene sheets for lithium-ion battery anodes. *ACS Nano* **10**(9), 8526–8535 (2016)
26. J. Deng, H. Li, S. Wang, D. Ding, M. Chen, C. Liu, Z. Tian, K.S. Novoselov, C. Ma, D. Deng, X. Bao, Multiscale structural and electronic control of molybdenum disulfide foam for highly efficient hydrogen production. *Nat. Commun.* **8**, 14430 (2017)
27. K. Zhang, M. Wang, X. Ma, H. Zhang, S. Hou, J. Zhao, X. Li, L. Qiang, Y. Li, Three dimensional molybdenum oxide/polyaniline hybrid nanosheet networks with outstanding optical and electrochemical properties. *New J. Chem.* **41**(19), 10872–10879 (2017)
28. Y. Liu, X. Wang, X. Song, Y. Dong, L. Yang, L. Wang, D. Jia, Z. Zhao, J. Qiu, Interlayer expanded MoS<sub>2</sub> enabled by edge effect of graphene nanoribbons for high performance lithium and sodium ion batteries. *Carbon* **109**, 461–471 (2016)
29. Z. Shi, W. Kang, J. Xu, Y. Sun, M. Jiang, T. Ng, H. Xue, D.Y.W. Yu, W. Zhang, C. Lee, Hierarchical nanotubes assembled from MoS<sub>2</sub>-carbon monolayer sandwiched superstructure nanosheets for high-performance sodium ion batteries. *Nano Energy* **22**, 27–37 (2016)
30. F. Zheng, Q. Pan, C. Yang, X. Xiong, X. Ou, R. Hu, Y. Chen, M. Liu, Sn-MoS<sub>2</sub>-C@C microspheres as a sodium-ion battery anode material with high capacity and long cycle life. *Chem.-Eur. J.* **23**(21), 5051–5058 (2017)
31. W. Ryu, J. Jung, K. Park, S. Kima, I. Kim, Vine-like MoS<sub>2</sub> anode materials self-assembled from 1-D nanofibers for high capacity sodium rechargeable batteries. *Nanoscale* **6**(19), 10975–10981 (2014)
32. K.J. Huang, L. Wang, J.Z. Zhang, K. Xing, Synthesis of molybdenum disulfide/carbon aerogel composites for supercapacitors electrode material application. *J. Electroanal. Chem.* **752**, 33–40 (2015)
33. C. Zhu, X. Mu, P.A. van Aken, Y. Yu, J. Maier, Single-layered ultrasmall nanoplates of MoS<sub>2</sub> embedded in carbon nanofibers with excellent electrochemical performance for lithium and sodium storage. *Angew. Chem. Int. Ed.* **53**(8), 2152–2156 (2014)
34. Y. Lu, Q. Zhao, N. Zhang, K. Lei, F. Li, J. Chen, Facile spraying synthesis and high-performance sodium storage of mesoporous MoS<sub>2</sub>/C microspheres. *Adv. Funct. Mater.* **26**(6), 911–918 (2016)
35. X. Zhang, X. Li, J. Liang, Y. Zhu, Y. Qian, Synthesis of MoS<sub>2</sub>@C nanotubes via the kirckendall effect with enhanced electrochemical performance for lithium ion and sodium ion batteries. *Small* **12**(18), 2484 (2016)
36. H. Miguez, F. Meseguer, C. Lopez, A. Blanco, J.S. Moya, J. Requena, A. Mifsud, V. Fornes, Control of the photonic crystal properties of fcc-packed submicrometer SiO<sub>2</sub> spheres by sintering. *Adv. Mater.* **10**(6), 480 (1998)
37. X. Huang, J. Chen, Z. Lu, H. Yu, Q. Yan, H.H. Hng, Carbon inverse opal entrapped with electrode active nanoparticles as high-performance anode for lithium-ion batteries. *Sci. Rep.* **3**, 2317 (2013)
38. H. Liu, D. Su, R. Zhou, B. Sun, G. Wang, S.Z. Qiao, Highly ordered mesoporous MoS<sub>2</sub> with expanded spacing of the (002) crystal plane for ultrafast lithium ion storage. *Adv. Energy Mater* **2**(8), 970–975 (2012)
39. A.C. Ferrari, J.C. Meyer, V. Scardaci, C. Casiraghi, M. Lazzeri, F. Mauri, S. Piscanec, D. Jiang, K.S. Novoselov, S. Roth, A.K. Geim, Raman spectrum of graphene and graphene layers. *Phys. Rev. Lett.* **97**(18), 187401 (2006)
40. X. Huang, Z. Zeng, H. Zhang, Metal dichalcogenide nanosheets: preparation, properties and applications. *Chem. Soc. Rev.* **42**(5), 1934 (2013)
41. H. Li, Q. Zhang, C.C.R. Yap, B.K. Tay, T.H.T. Edwin, A. Olivier, D. Baillargeat, From bulk to monolayer MoS<sub>2</sub>: evolution of raman scattering. *Adv. Funct. Mater.* **22**(7), 1385–1390 (2012)
42. J. Kibsgaard, Z. Chen, B.N. Reinecke, T.F. Jaramillo, Engineering the surface structure of MoS<sub>2</sub> to preferentially expose active edge sites for electrocatalysis. *Nat. Mater.* **11**, 963–969 (2012)
43. X. Liu, J. Liu, D. Zhan, J. Yan, J. Wang, D. Chao, L. Lai, M. Chen, J. Yin, Z. Shen, Repeated microwave-assisted exfoliation of expandable graphite for the preparation of large scale and high quality multi-layer graphene. *RSC Adv.* **3**(29), 11601–11606 (2013)
44. X. Liu, D. Chao, Q. Zhang, H. Liu, H. Hu, J. Zhao, Y. Li, Y. Huang, J. Lin, Z.X. Shen, The roles of lithium-philic giant nitrogen-doped graphene in protecting micron-sized silicon anode from fading. *Sci. Rep.* **23**, 15665–15669 (2015)
45. Y. Ding, P. Kopold, K. Hahn, P.A. Aken, J. Maier, Y. Yu, A lamellar hybrid assembled from metal disulfide nanowall arrays anchored on a carbon layer: in situ hybridization and improved sodium storage. *Adv. Mater.* **28**(35), 7774–7782 (2016)
46. X. Wang, Q. Weng, Y. Yang, Y. Bando, D. Gotberg, Hybrid two-dimensional materials in rechargeable battery applications and their microscopic mechanisms. *Chem. Soc. Rev.* **45**(15), 4042–4073 (2016)
47. Y. Liu, Y. Li, H. Kang, T. Jin, L. Jiao, Design, synthesis, and energy-related applications of metal sulfides. *Mater. Horiz.* **3**(5), 402–421 (2016)
48. R. Shidpour, M. Manteghian, A density functional study of strong local magnetism creation on MoS<sub>2</sub> nanoribbon by sulfur vacancy. *Nanoscale* **2**(8), 1429–1435 (2010)